Distinction between small RNA-bound and free ARGONAUTE via an N-terminal protein-protein interaction site

Simon Bressendorff[1,4], Ida Marie Zobbe Sjøgaard[1,4], Emilie Duus Oksbjerg[1], Swathi Kausika[1], Alec Michels[1], Andreas Prestel[2], Birthe B. Kragelund[2], Christian Poulsen[1,3] and Peter Brodersen[1,5]

[1]Copenhagen Plant Science Center, University of Copenhagen

[2]Structural Biology and NMR Laboratory, Department of Biology, University of Copenhagen

[3]Present address: Novo Nordisk A/S,

[4]These authors contributed equally to this work

[5]Corresponding author, email pbrodersen@bio.ku.dk

Abstract

ARGONAUTE (AGO) proteins bind to small non-coding RNAs to form RNA Induced Silencing Complexes (RISCs). In the RNA-bound state, AGO proteins are stable while RNA-free AGOs undergo regulated proteolysis or associate with chaperones *en route* to RISC maturation. Molecular determinants unique to RNA-free AGO that allow its specific recognition and degradation remain poorly characterized. Here, we show that the Arabidopsis autophagy cargo receptor ATI1 interacts with unloaded AGO1 via multiple interaction sites that include direct contact to a confined, linear region in AGO1, the N-coil. The N-coil is accessible to antibodies preferentially in the RNA-free state of AGO1, and influences its degradation rate *in vivo*. These results provide insight into the molecular basis for specific recognition of the RNA-free state of eukaryotic AGO proteins, and introduce a new tool for its further study.

Introduction

RNA Induced Silencing Complexes (RISCs) are central components in the processing of genetic information in eukaryotes. The minimal RISC consists of an ARGONAUTE (AGO) protein bound to a small non-coding RNA that guides RISC to complementary target RNAs by base pairing. In turn, RISCs repress gene expression sequence-specifically using a variety of mechanisms operating at either transcriptional or post-transcriptional levels. The exact properties of RISCs in these contexts are determined by several factors including the identity of the AGO protein, RISC co-factors, and the degree of small RNA:target RNA base pairing[1]. In animals, two distinct phylogenetic clades of AGO proteins exist. The Piwi clade is primarily used for silencing of transposable elements in the germline via Piwi-interacting RNAs (piRNAs)[2]. The Ago clade carries out endogenous gene regulation, in the main via microRNAs (miRNAs)[3], and, in particular in invertebrates, basic antiviral defense via virus-derived small interfering RNAs (siRNAs)[4]. Plants encode only Ago-clade proteins, and use several distinct, functionally specialized AGO proteins. For example, the AGO4/6/9 clade binds to siRNAs from transposable elements to form RISCs that affect transcriptional silencing by directing DNA methylation[5]. miRNAs mediate post-transcriptional regulation via cleavage or translational repression of mRNAs mainly in association with AGO1 with additional specialized, yet important, roles of AGO2, AGO7 and AGO10 (reviewed in [6]). Finally, antiviral RNA interference is carried out by AGO1, AGO2 and AGO5, and, potentially, by several additional AGO proteins[7-11].

All AGO proteins consist of four separate domains called N, PAZ, MID and Piwi[1]. They fold into a two-lobed structure in the small RNA-bound state with N and PAZ together in one lobe and MID/Piwi in the other[12-15] (Fig. 1). The ends of the small RNA are tethered in dedicated binding pockets in the MID and PAZ domains such that the 5'-end is bound to MID[16,17] and the 3'-end to PAZ[18]. PAZ and MID are connected by a long linker sequence called L2 that also interacts extensively with the small RNA backbone and with other AGO domains in the small RNA-bound state[13-15] (Fig. 1).

The assembly of RISC by incorporation of a small RNA into AGO, referred to as "RISC loading", is a critical event in all RNA silencing pathways. This process requires the Hsp40-Hsp70-Hsp90 chaperone assembly line in such a way that association of unloaded AGO with chaperones extends the dwell time of encounters between AGO and small RNA duplexes[19-23]. The chaperone assistance vastly increases the probability of a small RNA

duplex:AGO encounter to lead to formation of a long-lived AGO:small RNA duplex intermediate that subsequently matures into RISC with a single-stranded RNA by duplex unwinding[23], sometimes requiring passenger strand cleavage catalyzed by AGO[24-27]. The loading process constitutes a key regulatory point in RNA silencing. First, it is rate-limiting for biogenesis of many miRNAs *in vivo*[28]. Second, in many organisms including mammals, *C. elegans, Drosophila* and *Arabidopsis*, it is decisive for the stability of AGO proteins. Small RNA-bound AGO (RISC) is stable, but unloaded AGO is rapidly degraded *in vivo*[29-31], unless it exists as an Hsp90 complex *en route* to loading[31,32]. Although it is clear that both the ubiquitin-proteasome pathway and selective autophagy are involved in turnover of unloaded AGO both in plants and animals[29-34], two key questions remain poorly elucidated: (1) What are the molecular determinants that distinguish loaded from unloaded AGO to allow selective degradation of unloaded AGO? (2) What is the biological importance of eliminating unloaded AGO?

The first question has been approached in studies of the *Drosophila* miRNA effector Ago1, whose unloaded form is ubiquitinated in the L2 region by the RING finger protein Iruka[35]. This finding highlights L2 as a region of importance for distinction between loaded and unloaded AGO. It is, however, unlikely to be easily generalized to other systems, because the site of ubiquitination is non-conserved, and, in particular, is adjacent to a *Dm*Ago1-specific deletion in L2 compared to other miRNA-interacting AGO proteins (Supplemental Fig. 1). The second question remains unresolved, but it is widely assumed that avoidance of loading of RNA degradation fragments into AGO that may initiate unwanted RISC-mediated repression or compete with *bona fide* miRNAs for AGO binding is a major driver of mechanisms targeting unloaded AGO for proteolysis[29,30,35]. This hypothesis is indirectly supported by several lines of evidence, although clear observations of ectopic or reduced RISC function upon inactivation of factors involved in AGO degradation have not been reported. For example, mutation of the *Arabidopsis* F-box protein FBW2 restores steady-state levels of an AGO1 mutant protein predicted to have a destabilized fold of the PAZ domain[36]. It is, however, unclear whether FBW2 targets AGO1 directly, and whether it specifically mediates degradation of unloaded, but functional AGO1, or plays a more general role in chaperone-assisted protein degradation elicited as a consequence of partial unfolding of the PAZ domain in the point mutant analyzed. In addition, mutations in key components of miRNA biogenesis had to be introduced to observe relatively minor

changes in populations of AGO1-loaded small RNAs upon inactivation of *FBW2*, and no causal relationships between illegitimate siRNAs bound to AGO1 and phenotypes could be established[36]. Similarly, the efficiency of miRNA-guided target mRNA repression was only modestly reduced in *Drosophila* S2 cells upon depletion of Iruka[35].

In this study, we use the *Arabidopsis* miRNA effector AGO1 to define a region of crucial importance in the distinction between eukaryotic AGO proteins in the RNA-bound and in the free state. We show that the N-coil, a small, highly conserved linear region towards the N-terminus of AGO1, yet part of the MID-Piwi lobe in the loaded conformation, is preferentially accessible in unloaded AGO1. Furthermore, the N-coil functions as a direct binding site for the autophagy cargo receptor ATG8 INTERACTING PROTEIN1 (ATI1). This highlights the N-coil as a key determinant of the distinction between loaded and unloaded AGO1, and, given its conservation and structural properties, probably in other eukaryotic AGO proteins in both Ago and Piwi clades.

Results

Definition and properties of structural units of the N-terminal part of AGO1

Arabidopsis thaliana (At) AGO1 has a 176-aa extension at its N-terminus, in addition to the canonical N-PAZ-MID-PIWI domains found in all AGO proteins. Because this extension is predicted to be an intrinsically disordered region (IDR, Supplemental Fig. 2), we term this part of AGO1 the N-IDR. The N-IDR is followed by a 14-aa region (F177-K190) that we previously termed the N-coil[6]. The N-coil is of interest for a number of reasons: (i) Despite its location in the N-terminal part of AGO in sequence, it is part of the MID-PIWI lobe in structures of AGO-small RNA complexes (Fig. 1a,b). (ii) The N-coil assumes an extended conformation with no secondary structure, yet has low structural flexibility, and reaches across the width of the entire AGO-small RNA complex (Fig. 1b). (iii) Residues in the conserved N-coil are structurally fixed by numerous inter-domain interactions in the AGO-small RNA complex, and the N-coil interface is only moderately hydrophobic with several residues calculated to prefer a hydrophilic environment (Fig. 1c). For example, R182 participates in a salt bridge deep inside of the PIWI domain (Fig. 1d), perhaps suggesting that the conformation of the N-coil revealed in the crystal structures of AGO-small RNA complexes is but one of several possible conformations of this region. (iv) The N-coil is functionally important because two mutations in this region have been recovered in forward

screens in plants: *ago1-38* (G186R) that exhibits relatively weak loss of function, and shows lower abundance in membrane compartments compared to wild type[37,38], and *ago1-55* (G189E) that exhibits stronger loss of AGO1 function[39]. The N-coil is followed by two β-strands and the globular N-domain (Fig. 1b). The key functional importance of the N-coil and the connecting β-strands is underscored by the observation that substitution of this part of the catalytically inactive human Ago1 by the corresponding part of the catalytically active Ago2 is sufficient to confer activity on an Ago1 variant containing all four residues required for coordination of the two catalytic metal ions[40]. Despite these indications of functional importance of the N-coil region, the precise functions of the entire N-coil-Globular N (NcGN) part of AGO proteins remain ill-defined. Functions of the globular N-domain itself are particularly poorly understood, although the absence of mutations recovered in this part in forward genetic screens reporting on siRNA/miRNA function in plants hints that its functions are not central to the core biochemical properties such as small RNA binding and target RNA cleavage[6].

The N-coil-Globular N part of AGO1 interacts with multiple factors implicated in regulated proteolysis and functions as a degron

To reveal functions of the poorly understood NcGN part of Arabidopsis AGO1, we first conducted yeast two-hybrid screens with NcGN as a bait against three prey cDNA libraries. This effort yielded 15 potential AGO1-NcGN interactors, all validated in the two-hybrid system by isolation of the prey plasmid and re-transformation with AGO1 NcGN bait into the reporter strain (Supplemental Fig. 3, Table S1). Several candidate interactors had predicted biochemical functions related to regulated proteolysis via either the ubiquitin-proteasome pathway or via autophagy (Table S1). This also included the two intrinsically disordered, transmembrane autophagy cargo receptor proteins ATI1 and ATI2[41,42] that were previously shown to be implicated in degradation of AGO1 via the poleroviral RNAi suppressor P0[43]. The trend towards protein degradation was not exclusive, however, as other interactors were also recovered, including Hsp90, a protein phosphatase, and vesicle trafficking and membrane contact proteins (VAP27, NTMC2T5.1)[44,45] (Table S1). Nonetheless, since "Regulated proteolysis" was the clearest common functional category among candidate interactors, we carried out pulse labeling experiments with yellow fluorescent protein (YFP) and NcGN-YFP fusions stably expressed in *Arabidopsis thaliana* to see whether the NcGN

in isolation could cause rapid degradation. When lines with similar YFP steady state levels were compared, the synthesis rate (and hence also the degradation rate) of the NcGN-YFP fusion protein was indeed 6.6-fold higher than YFP alone, demonstrating that the NcGN is subject to rapid proteolysis (Supplemental Fig. 4). We note that recognition of NcGN by the chaperone-assisted protein degradation machinery as a consequence of its detachment from normally interacting domains in native AGO1 is unlikely, because the $Gal4^{BD}$-NcGN fusion protein was easily detectable in yeast (Supplemental Fig. 4), and was sufficiently stable for yeast two-hybrid analyses to be carried out. Thus, we focused our attention on the role of the NcGN in regulated proteolysis of the AGO1 protein.

Most candidate NcGN interactors are specific for AGO1

The AGO protein family contains 10 paralogs in Arabidopsis, of which AGO4 is distantly related while AGO10 is very closely related to AGO1. We therefore first used the NcGNs of AGO4 and AGO10 to test whether a subset of the identified candidate interactors (ATI1, ATI2, AUF1, AUF3, UBI, HUB1, PP2C and Hsp90-3, see Table S1) were specific to the NcGN of AGO1 or whether they represented generic AGO NcGN binding proteins. Seven of the candidates (ATI1, ATI2, AUF1, AUF3, UBI, HUB1, PP2C) showed yeast two-hybrid interactions preferentially or exclusively with the NcGN of AGO1, while one (Hsp90-3) interacted with the NcGN of all three proteins (Fig. 2a, Supplemental Fig. 5). These results indicate that most of the candidate interactors isolated by yeast two-hybrid screening are specific to AGO1. We also note that the more general AGO NcGN interaction observed with Hsp90-3 is consistent with the involvement of Hsp90 in the loading of different AGO proteins across organisms[19-21].

The N-coil is of special importance for interactions via the NcGN

Since two mutations with functional impact have been identified in the N-coil of AGO1 (G186R, G189E) [37,39], we tested whether the 14-aa N-coil may play a role in binding to some of the interactors. We initially screened the interactors for ability to interact with the NcGN carrying the G186R mutation. Surprisingly, this point mutation in the N-coil resulted in strongly reduced interaction with most candidates as measured by β-galactosidase activity originating from *lacZ* expressed under UAS_{Gal} control in the reporter strain (Fig. 2b). Indeed, of five proteins tested (ATI1, ATI2, TCTP, AUF1 and Hsp90) only Hsp90 and AUF1 showed

clear interaction upon deletion of the N-coil (Supplemental Fig. 6). On the other hand, with the exception of Hsp90, the N-coil was not sufficient for interaction with any candidate (Supplemental Fig. 6). Because these results point to a special importance of the 14-aa N-coil in several protein-protein interactions, we focus the remainder of the study on defining the properties of the N-coil that underlie its importance in protein-protein interactions involving AGO1. To this end, we chose the NcGN-mediated interaction with the transmembrane ATI1 and ATI2 proteins as our model system, and focused on the IDRs of those proteins, because they define their cytoplasmic part[42]. Furthermore, conditions for their heterologous expression and purification have been established [42].

Mapping of residues important for ATI1/ATI2 interaction across the entire NcGN

To identify amino acid residues in the AGO1 NcGN required for ATI1/2 interaction, we first inspected alignments between AGO1 orthologues from many different plant species and between *Arabidopsis* AGO1 and its closest paralogue, AGO10 (Fig. 3a). This analysis revealed multiple sites of variation between AGO1 and AGO10 concentrated in the N-coil and in distinct sites in the GN-domain (Fig. 3a). Several of these sites corresponded to surface-exposed patches, consistent with an involvement in protein-protein interaction (Fig. 3b). We therefore constructed a series of point mutants in AGO1 NcGN residues variable between AGO1 and AGO10, and tested the interaction in the yeast two-hybrid system with ATI1 and ATI2. The results showed that multiple residues in the N-coil (K178, K185, K190) and in a few surface-exposed patches of the globular N-domain (P259, M304/E307, especially E307) are required for interaction with ATI1/2 (Fig. 3c, Supplemental Fig. 7-8). In particular, mutation of either lysine residue to glutamic acid throughout the N-coil (K178E, K185E, K190E) disrupted the NcGN-ATI interaction. We therefore moved on to assess the effect of these residues more quantitatively, and to test whether they interacted directly with the IDR of ATI1.

The K178E N-coil mutation decreases the NcGN:ATI1-IDR affinity by about 4-fold

We first expressed and purified the IDR of ATI1[42] and wild type and K178E mutant versions of the NcGN of AGO1 fused to SUMO (Fig. 4a), and used these purified proteins for quantitative binding assays by microscale thermophoresis. This assay uses the distinct thermophoretic mobility of different molecular entities to measure the percentage of complex

formed between a fluorescently labeled component, and a partner protein added in increasing concentrations from none (0% complex) to an estimated 100-fold molar excess (~100% complex). In our experimental set-up, His_6-SUMO-AGO1 NcGN (WT or K178E) was fluorescently labeled on the unique Cys192 residue close to the N-coil, and the unlabeled IDR of ATI1 was added in increasing quantities. Using this set-up, we confirmed that the interaction between AGO1 NcGN and ATI1-IDR is direct, and measured the dissociation constant to be 11±2 μM (Fig. 4b). Remarkably, these affinity measurements did not necessitate application of a thermal field to measure differential molecular movement, because the fluorescence intensity itself was sensitive to addition of ATI1 (Fig. 4c). This observation suggests that in the AGO1 NcGN-ATI1-IDR complex, the C192-linked fluorophore is located in a distinct chemical environment compared to the free AGO1 NcGN, and thus, close to an interaction site. Indeed, when the N-coil mutant K178E was analysed in the same assay, both the affinity of the ATI1-IDR interaction (47±12 μM), and, especially, the change of fluorescence upon complex formation were substantially reduced (Fig. 4b,c). Taken together with the results of the mutational analyses conducted using yeast two-hybrid assays, these observations indicate that the N-coil is a direct site of interaction between AGO1-NcGN and ATI1-IDR, and that it contributes substantially to the affinity of the interaction.

Residues in the N-coil interact directly with the IDR of ATI1

To show conclusively that the N-coil is a direct interaction site of ATI1-IDR, we expressed and purified an ^{15}N-labeled N-coil peptide (172-SSSKAFKFPMRPGKGQSGKRC-192) to perform 2D ^{1}H-^{15}N heteronuclear single quantum coherence nuclear magnetic resonance (NMR) spectroscopy in the presence and absence of the ATI1-IDR. These experiments showed that the signal intensities from backbone amide N-H nuclei of several residues in the N-coil, in particular the N-terminal part from F177-K185, and to a lesser extent the C-terminal K190, were strongly reduced upon addition of ATI1-IDR (Fig. 4d,f), indicating that these residues participate directly in the interaction. Consistent with the importance of K178 for the ATI1-IDR interaction, such loss of signal was markedly less pronounced upon addition of ATI1-IDR to an ^{15}N-labeled N-coil peptide containing the K178E mutation, in particular for the amide group of residue 178 (K/E) itself (Fig. 4d-h). We conclude that the N-coil is a direct interaction site of the ATI1-IDR, and that the interaction involves contacts

along the entire N-coil, including the K178, K185, and K190 residues. This is noteworthy, because these residues are not spatially close in the high-confidence Alphafold structure of AGO1 in the small RNA-bound conformation (Fig. 3b). Rather, the positions of these residues span the entire width of AGO1, and, given the close N-coil-Piwi domain contacts, define a large surface area of AGO1 in this conformation (Fig. 1a,b). Taken together with the observation that each of these lysines contributes measurably to the interaction (Fig. 3-4, Supplemental Fig. 7), it is a plausible hypothesis that in the ATI1-interacting conformation of AGO1, the N-coil is detached from the remainder of the AGO1 protein, i.e. different from the small RNA-bound conformations captured by X-ray crystallography. We therefore moved on to study the AGO1-ATI1-IDR interaction in the context of full length AGO1, and set out to include analyses of both small RNA-bound and free AGO1.

ATI1 interacts with unloaded AGO1 in vivo and the binding implicates N-coil residues

To generate small RNA-free AGO1, we engineered the Y691E mutant, mutated in a key residue in the MID domain that stacks with the 5'-uridine ring of the small RNA, and coordinates the 5'-phosphate of the small RNA. In other Ago proteins, the equivalent mutation leads to complete loss of small RNA binding[34,46]. We used stable transgenic lines in *Arabidopsis* to establish that the Y691E mutant indeed is unloaded. When expressed in the *ago1-3* knockout background, the mutant protein failed to rescue the knockout mutant phenotype, demonstrating total loss of function (Supplemental Fig. 9). In addition, immunoprecipitation of wild type and Y691E mutant protein followed by polynucleotide kinase-mediated labeling of co-purified small RNA showed that in contrast to $AGO1^{WT}$, no small RNA was bound by the $AGO1^{Y691E}$ protein (Supplemental Fig. 9).

Because heterologous expression of AGO1 failed, even with the use of a variety of expression hosts (*E. coli*, baculovirus/*Sf-9*, *Schizosaccharomyces pombe*) and affinity/solubilization tags, we used bimolecular fluorescence complementation (BiFC) assays upon transient expression in *Nicotiana benthamiana* for assessment of ATI1 interaction with $AGO1^{WT}$ and $AGO1^{Y691E}$. The close AGO1 paralogue, AGO10, was used as a negative control. With $AGO1^{WT}$ fused to the C-terminal part of YFP and ATI1 fused to its N-terminal part (C-YFP-$AGO1^{WT}$ and N-YFP-ATI1), weak, but specific signal was detected in association with the endoplasmic reticulum (ER; Fig. 5a), consistent with previous reports of ATI1-localization to ER-associated ATI-bodies, and with peripheral ER-association of

AGO1 [47,48]. We detected a consistent and statistically significant reduction in intensity of the BiFC signal when the C-YFP-AGO1$^{K185E/K190E}$ mutant containing substitutions in N-coil residues implicated in ATI1 binding was used (Fig. 5a,b; Supplemental Fig. 10). We next compared patterns of BiFC signal obtained with C-YFP-AGO1^{Y691E}/N-YFP-ATI1 and C-YFP-AGO1$^{Y691E/K185E/K190E}$/N-YFP-ATI1. With both forms, specific signal was detected, and, similar to what we observed with the wild type AGO1 capable of small RNA binding, the K185E/K190E N-coil mutations resulted in significantly reduced BiFC signal intensity (Fig. 5a,b). These results demonstrate that ATI1 interacts with the unloaded form of AGO1, and that N-coil residues contribute to this interaction *in vivo*. We note that complete disruption of ATI1-AGO1 interaction is not expected upon mutation of N-coil residues, because a previous study showed yeast two-hybrid interactions between ATI1 and AGO1 involving both N-PAZ and MID-Piwi lobes of the protein[43]. We also note that the results show that ATI1 is capable of interacting with unloaded AGO1, and may possibly only interact with the unloaded form, because wild type AGO1 exists as a mixed population *in vivo*, mostly of the RNA-bound form, but also with a minor fraction in the unloaded form (see below). Clearly, however, such possible exclusive interaction with unloaded AGO1 is not established by the BiFC assays.

Defective ATI1 interaction sites in the NcGN reduce the degradation rate of unloaded AGO1

We next asked whether the interaction sites in the AGO1 NcGN defined by our analyses thus far had an effect on the turnover of unloaded AGO1 *in vivo*. We first generated stable transgenic plants constitutively expressing NcGN-YFP fusions with or without mutations found to disrupt ATI1/ATI2 binding. The AGO1-NcGN wild type construct was also expressed in *ati1/ati2* double knockout backgrounds (Supplemental Fig. 11) to test the possible implication of these two specific NcGN interactors in the turnover of AGO1. Comparisons of NcGN^{WT}-YFP, NcGN$^{K178E/K185E/K190E}$-YFP and NcGN$^{K178E/K185E/K190E/P259E/M304E/E307A}$ protein and mRNA levels showed that the NcGN mutants indeed had higher protein/mRNA ratios than their wild type counterpart (Fig. 6a, Supplemental Fig. 11). This effect could not be explained by different YFP siRNA levels (Supplemental Fig. 11), and is therefore consistent with slower protein degradation *in vivo*. Higher protein/mRNA ratios were also found for AGO1 NcGN in the *ati1*/*ati2* knockout background compared to wild type, although the effect was less pronounced than with NcGN mutants, as expected. Thus, we moved on to test the relevance of the NcGN for degradation

of the full-length, unloaded AGO1 protein using pulse-labeling analysis to extract kinetic information directly. To maximize chances of measuring an effect *in vivo*, we used the K185E/K190E/M304E/E307A (henceforth, KKME) mutant with residues important for ATI1/2 interaction substituted both in the N-coil and in the globular N-domain. Thus, stable transgenic lines expressing equal steady-state levels of FLAG-AGO1^{WT}, FLAG-AGO1^{Y691E}, and FLAG-AGO1$^{Y691E/KKME}$ were selected as material for kinetic analyses (Supplemental Fig. 12). We first considered the possible kinetic pathways of newly synthesized AGO1^{WT} and AGO1^{Y691E}. Because AGO1^{WT} can be degraded either prior to or after small RNA loading, (Fig. 6b), the labeling data must be fitted to a sum of two exponentials, with half-lives corresponding to unloaded (minor fraction, 8.5±1.8%, see Methods) and loaded states (major fraction, 91.5±1.8%, see Methods), respectively. In contrast, labeling of the unloaded AGO1^{Y691E} is expected to follow mono-exponential kinetics. Initial analyses indicated that ^{35}S-Met/Cys labeling of entire seedlings resulted in uniform distribution of label within 15 minutes (Supplemental Fig. 13), but that a classical pulse-chase set-up was not feasible, because incorporation continued after addition of the chase. Since synthesis and degradation rates are equal at steady state, we decided to do pulse-labeling experiments and measure protein half-lives from incorporation rates of ^{35}S-label/total AGO1 protein in FLAG immunoprecipitations following addition of ^{35}S-Met/Cys label (see Methods). We first compared FLAG-AGO1^{WT} and FLAG-AGO1^{Y691E} lines expressing comparable levels of FLAG-AGO1 at steady state (Fig. 6c,d). This analysis showed that wild type AGO1 indeed exhibits two-phase kinetic behavior. Gratifyingly, the half-life of the rapid phase roughly matches that of unloaded AGO1 measured with the Y691E mutant [$t_{1/2}$(WT, rapid) = 1.6±0.6 h, $t_{1/2}$(Y691E) = 2.5±0.5 h]. We therefore repeated the pulse-labeling experiments with wild type and NcGN interaction site mutants in the unloaded FLAG-AGO1^{Y691E} version, i.e. FLAG-AGO1^{Y691E} vs FLAG-AGO1$^{Y691E/KKME}$. These experiments showed a modest, but reproducible reduction in degradation rate of the mutant with the defective NcGN interaction site (Fig. 6c,e; results of two independent experiments shown to convey their quantitative variability). We conclude that intact NcGN interaction sites, including the N-coil, are necessary for maximal turnover rates of unloaded AGO1 *in vivo*.

The N-coil is uniquely accessible in unloaded AGO1

The results presented thus far establish that residues in the N-coil make direct contacts to the ATI1-IDR, that the ATI1-IDR can interact with the RNA-free state of AGO1, and that ATI1-IDR interaction sites in the NcGN of unloaded AGO1 contribute measurably, if modestly, to its rapid turnover *in vivo*. Because of the unique structural properties of the N-coil, we hypothesized that this part of AGO proteins could be a site with substantially altered accessibility between loaded and unloaded conformations of AGO that would allow specific recognition of unloaded AGO for degradation. To test this hypothesis, we raised antibodies against a 16-aa N-coil peptide (F177-C192). This polyclonal antibody specifically recognized the N-coil as demonstrated by its clear reactivity towards FLAG-immuno-purified, denatured AGO1 with a wild type N-coil, but substantial loss of reactivity with FLAG-AGO1 carrying the K185E/K190E mutations in the N-coil (Fig. 7a,b). We next used this antibody to probe the accessibility of the N-coil in AGO1 in two different ways. First, we observed that binding of equal amounts of N-coil antibody required 10-fold higher amounts of immuno-purified, native, immobilized FLAG-AGO1^{WT} (largely small RNA-bound) than of similarly purified unloaded AGO1 (FLAG-AGO1^{Y691E}) (Fig. 7b,c). We note that this difference cannot be explained by potentially different patterns of post-translational modifications in the N-coil, because the antibody recognized denatured forms of the two AGO1 variants equally efficiently (Fig. 7b). Second, direct immunoprecipitation from total lysates using the N-coil antibody resulted in markedly more efficient recovery (~10 fold) of FLAG-AGO1^{Y691E} than of FLAG-AGO1^{WT} (Fig. 7d), in contrast to the result obtained with FLAG antibodies (Fig. 7b). These observations provide clear evidence that the N-coil of AGO1 is preferentially accessible in the unloaded state.

Conformational flexibility of the N-coil is widespread in eukaryotic Ago- and Piwi-clade proteins

We finally inspected existing structural data on eukaryotic AGO proteins both of the Ago and Piwi clades for information on potential structural flexibility of the N-coil, if possible dependent on the loading status. The structures of the human miRNA-associated Ago proteins, Ago1-Ago4 in the loaded state all show the N-coil in a nearly identical conformation firmly associated with the Piwi domain as depicted in Fig. 1, and are, therefore, not informative in this regard. However, several regions of differential solvent exposure between RNA-free and guide RNA-associated human Ago2 can be identified from recent data on

hydrogen-deuterium exchange rates in these two states [49] (Fig. 8a). These include the N-coil and, in particular, the nearby hydrophilic environment caging the guanidium group of the conserved R182 side chain in the RNA-bound state (Fig. 1a). This observation on HsAgo2 extends the conclusion reached here with AtAGO1 that the N-coil assumes different conformations depending on the loading status of AGO.

In the Piwi-clade, three structures of piRNA-bound proteins are available: silkworm (*Bombyx mori*) Siwi, *Drosophila melanogaster* (Dm) Piwi, and the sea sponge *Ephydatia fluviatilis* (Ef) Piwi. The Siwi structure shows an N-coil from I130 to G148 (ISILRTRPEAVTSKKGTSG) associated with the MID-Piwi lobe much like in Ago-clade structures, while *Ef* Piwi shows a partial and *Dm* Piwi no N-coil at all (Fig. 8b), presumably due to proteolytic cleavage prior to crystallization. These indications of facultative association of Piwi-clade N-coils with the MID-Piwi lobe domain suggest that the N-coil exhibits conformational flexibility, perhaps accompanying conformational differences of the proteins upon piRNA binding, as in the case of Ago-clade AGO proteins. Strikingly, the compactness of the Piwi:piRNA complexes increases progressively from the *Dm* Piwi structure (no N-coil present) to the Siwi structure (full N-coil present) (Fig. 8b,c), lending support to the idea that the N-coil/MID-Piwi lobe association is an important step in reaching the final conformation of mature RISC across both Piwi and Ago clades.

Discussion

Distinction between loaded and unloaded AGO via the N-coil

Our results demonstrate that the N-coil is exposed for interaction uniquely in the unloaded state of AGO1. This is important, because it defines a conformational change that accompanies the AGO loading process, and, thereby, confers distinct protein-protein interaction properties on the two forms of AGO. Three different aspects are worth further comments in this regard. First, as demonstrated here, it offers a precise molecular explanation to the longstanding observation that unloaded AGO proteins in plants and animals turn over much more rapidly than the small RNA-bound form. In *Arabidopsis*, this is illustrated by the identification of many interactors involved in regulated proteolysis, most clearly ATI1, that depend on the N-coil for interaction with the NcGN fragment of AGO1. Given the structural conservation of the N-coil in widely different AGO proteins, it is likely that this same molecular principle operates in many different organisms, and, thus,

contributes to the rapid turnover of unloaded AGO more generally. Second, because the N-coil is a recurrent structural element in all AGO proteins, including the Piwi clade, its exposure in unloaded forms may also explain other molecular properties distinct from rapid turnover of unloaded AGO. For instance, in insect germline cells, Piwi proteins engage in a so-called ping-pong amplification cycle of piRNAs derived from transposable elements. Ping-pong amplification entails cleavage of a sense piRNA precursor transcript by a mature piRISC containing the Piwi protein Aubergine (Aub) bound to a primary, anti-sense piRNA, and subsequent loading of the sense cleavage fragment onto another Piwi-clade protein, Ago3[50-52]. Ago3 is precluded from primary piRNA association by the protein Krimper that associates with Ago3 specifically in the free state[53]. The definition of the molecular determinants of the recognition of the unloaded state of Ago3 by Krimper remains incomplete[53], but it is now an obvious possibility that the N-coil of Ago3 is one of those determinants. Third, the demonstration that the N-coil becomes inaccessible to antibodies after loading reveals new insight into the molecular mechanics of the loading process itself. It is a reasonable interpretation of our data that attachment of the N-coil to the Piwi domain is a key step in reaching the compact conformation of the loaded structure observed in human Ago1-4, in particular via the salt bridge deep inside of the Piwi domain involving the universally conserved R182 in the Arabidopsis AGO1 N-coil. Our inspection of available Piwi protein structures lends support to this interpretation, because the compactness of the structures follows the degree of N-coil/MID-Piwi association, consistent with the N-coil acting as a zipper that holds the two lobes together in a compact conformation. Finally, we note that our identification of Hsp90 as an interactor of the N-coil also suggests a simple explanation for why chaperone interaction protects AGO proteins from rapid proteolysis. If the N-coil, and potentially other structural determinants with similar exclusive exposure in the unloaded state of AGO, are concealed via chaperone interaction, chaperone binding to an AGO protein would preclude its interaction with the factors targeting its unloaded form for proteolysis.

Possible roles of N-coil-mediated degradation of unloaded AGO1

While our study provides a clear answer to the question of how RNA-free AGO1 can be specifically targeted for rapid proteolysis, it does not provide insight into the biological importance of such clearance of unloaded AGO1. The most straightforward explanation for

the importance of rapid proteolysis of free AGO proteins is that it precludes loading of illegitimate small RNA species such as degradation fragments, and thereby eliminates potentially dangerous unwanted AGO-mediated gene repression and competition with *bona fide* regulatory small RNAs. Although this explanation is plausible, it may not be the only reason underlying the rapid degradation of free AGO proteins. Protection from loading of endogenous RNA degradation fragments is a fundamental molecular property required in the earliest ancestors in which AGO proteins are present, and the machinery responsible for degradation of unloaded AGO may therefore be expected to be deeply conserved in eukaryotes. However, with the exception of the histone ubiquitin ligase HUB1 and the Translationally Controlled Tumor Protein (TCTP), the AGO1 NcGN interactors isolated here are generally not conserved beyond plants, including proteins with roles in regulated proteolysis such as ATI1 and ATI2. Which additional factors may drive the evolution of systems to rapidly degrade unloaded AGOs? Since there is now evidence indicating that several plant and animal pathogens, including fungi, oomycetes, parasitic plants, and nematodes, use small RNAs as virulence factors [54-57], it is an attractive possibility that rapid proteolysis of unloaded AGO proteins also evolved as a protective mechanism to defend against those pathogens whose virulence is enhanced by reshaping host gene expression using secreted siRNAs. Clearly, the identification of the N-coil as a site of protein-protein interaction accessible only in RNA-free AGO should facilitate tests of this hypothesis across plant and animal kingdoms.

Figure legends

Fig. 1 | Structural properties and conserved interactions of the N-coil in Hs-Ago2. Overview of the Hs-Ago2 domain structure with surface outline of the globular N domain and the N-coil. **a**, “side view”; **b**, “bottom view”. **c**, Intra-molecular interactions between the N-coil and the remaining part of Hs-Ago2 as calculated by the Protein Interfaces, Surfaces and Assemblies service PISA[58]. The solvation energy gain of the N-coil is calculated as the difference between free energy of the associated and the dissociated N-coil. A negative solvation energy, $\Delta_i G$, of a residue makes a positive contribution to the solvation energy gain of the interface thus favoring the dissociated state. The color gradient (blue to red) indicates the effect sizes of buried surface area and solvation energy and highlights the unique properties of Arg-28. **d**, Inlet showing conserved residues and bonds between a

buried arginine side chain in the N-coil (R28 in Hs-Ago2) and nearby residues. Data and presentations were made using the crystal structure coordinates of the miR20a-bound Hs-Ago2 (PDB 4F3T)[15].

Fig. 2 | Interactions with AGO1-NcGN are specific and often require an intact N-coil. **a**, Yeast two-hybrid analysis of ATI1 and ATI2 fused to the activation domain (AD) of the yeast transcription factor Gal4 co-expressed either with NcGN domains of AGO1/AGO10/AGO4 fused to the DNA binding domain of Gal4 (BD), or with Gal4-BD alone (empty). 10-fold serial dilutions of yeast cells were spotted on permissive (left) and selective (right) media. **b**, β-galactosidase activity measured in an *ortho*-nitrophenyl-β-galactoside (ONPG) assay conducted with total protein lysates prepared from yeast strains expressing each candidate fused to Gal4-AD and AGO1-NcGN-Gal4-BD, AGO1-NcGN^{G186R}-Gal4-BD, or unfused Gal4-BD (empty). y-axis shows β-galactosidase activity in arbitrary units. The yeast Swi2-Swi6 interaction was used as positive control, and co-expression of unfused Gal4-AD and Gal4-BD was used as negative control.

Fig. 3 | Residues required for ATI1/ATI2 interaction cluster in the N-coil and in surface-exposed patches of the globular N-domain **a**, Sequence alignments of the *Arabidopsis* paralogs AGO1 and AGO10, and of orthologs of *Arabidopsis* AGO1 from plant species representing major phylogenetic groups of land plants. The species chosen from the different groups were as follows: Liverwort, *Marchantia polymorpha*; moss, *Ceratodon purpureus*; lycophyte, *Selaginella moellendorfii*; fern; *Ceratopteris richardii*; gymnosperm, *Pinus tabuliformis*; monocot, *Elaeis guineensis*; dicot, *Arabidopsis thaliana*. Residues selected for mutational analysis are marked on the alignment. **b**, Alphafold ribbon model of *Arabidopsis* AGO1 with the N-coil and N domain highlighted in rainbow colors. The residues studied by mutation are presented in sticks and colored according to the effect of mutation on ATI1/ATI2 interaction with AGO1-NcGN in the yeast two-hybrid assay. The underlying evidence from yeast-two hybrid spotting assays is shown in Supplemental Fig. 7-8.

Fig. 4 | The N-coil is a direct binding site for ATI1 *in vitro*. **a**, SDS-PAGE of heterologously expressed SUMO-AGO1-NcGN protein used for fluorescence labeling and microscale thermophoresis (MST) assays. **b**, MST measurements of fluorescence intensity

of SUMO-AGO1 NcGN WT (left) and K178E (right) after application of a temperature gradient. Fluorescence data obtained from the thermophoretic acquisition period were normalized to the initial fluorescence before being fitted to a one-site binding curve with increasing concentrations of ATI1-IDR. The reported binding constants (K_D) are calculated with standard errors. **c**, Simple fluorescence intensity of Cys192-labeled His_6-SUMO-AGO1 NcGN WT (left) and K178E (right) as a function of the concentration of ATI1-IDR. **d, e**, $^{1}H,^{15}N$-HSQC nuclear magnetic resonance spectra of 50 µM of ^{15}N-labeled AGO1 N-coil WT (left, black) or K178E peptide (right, black), with 19 µM ATI1-IDR added (green with N-coil WT, blue with N-coil K178E). Zooms of contour levels of residues K178 and C192 are highlighted in the boxes. Minor peaks indicated with asterisks were assigned to a C-terminally truncated version of the AGO1 N-coil peptide whose presence in the sample was verified by MALDI-TOF mass spectrometry. **f, g**, Peak intensity plots of ^{15}N-labeled AGO1 N-coil peptide (50 µM) upon titration of ATI1-IDR. Peak intensities are normalized to peak intensities observed with free AGO1 N-coil peptide. **h**, Peak intensity of residues K178 (for the AGO1 wild type N-coil, green) and E178 (for the K178E N-coil mutant, blue) as a function of the ATI1-IDR concentration. The data points were fitted to a one-site binding curve.

Fig. 5 | Unloaded AGO1 interacts with ATI1 *in vivo*. a, Confocal images showing results of bimolecular fluorescence complementation (BiFC) assays to probe the AGO1-ATI1 interaction *in vivo*. The C-terminal half of YFP was fused to AGO10, or to wild type or unloaded (Y691E) AGO1 with either an intact or a mutated (K185E/K190E) N-coil. The N-terminal half of YFP was fused to ATI1. Both fused halves of YFP were expressed from the same plasmid also expressing free RFP. For each BiFC pair, possible interaction is detected by fluorescence from reconstituted YFP. RFP fluorescence serves as a control for transformation. Merged channel images demonstrate the presence of yellow fluorescence only in transformed cells. Scale bar, 50 µm. **b**, Quantification of YFP signal normalized to RFP signal in the given number of YFP-positive cells for the interactions shown in a. Letters indicate groups with statistically significantly different $\log_2$(YFP/RFP) ratios ($p < 0.05$; ANOVA with post-hoc Tukey Honestly Significant Difference test). See Supplemental Fig. 9 for evidence that $AGO1^{Y691E}$ is unloaded, and Supplemental Fig. 10 for image data underlying the quantification in b.

Fig. 6 | An intact AGO1 N-coil is required for maximal turnover rate of unloaded AGO1 *in vivo*. **a**, Ratios of normalized YFP protein to YFP mRNA levels as quantified by protein and RNA blots in stable transgenic lines constitutively expressing AGO1 NcGN-YFP fusions, either in WT or in the *ati1-1/ati2* knock-out background. Ratios are normalized to AGO1-NcGN^{WT}-YFP expressed in WT. KKK, K178E/K185E/K190E; 6mut, KKK/P259E/M304E/E307A. **b**, Kinetic model of the two different fates of newly synthesized AGO1: direct degradation (κ_1), or small RNA loading (κ_2) followed by degradation (κ_3). **c**, Quantification of ^{35}S-Met/Cys incorporation into FLAG-AGO1^{WT}, FLAG-AGO1^{Y691E} or FLAG-AGO1$^{KKME/Y691E}$ as a function of pulse time. The lines represent a fit to an exponential equation for unloadable AGO1 containing the Y691E mutation and a fit to a double exponential equation for the WT AGO1. The half-lives calculated by the fitted models are given in hours +/- standard deviation, as detailed in Methods. **d**, Zoom in of the dashed area of **c**. **e**, Result of an independent experiment done as in **c** to verify the slower incorporation kinetics in FLAG-AGO1$^{KKME/Y691E}$ compared to FLAG-AGO1^{Y691E}. See Supplemental Fig. 11 for protein and RNA blot data underlying Fig. 6a, and Supplemental Fig. 12 for raw data underlying Fig. 6c-e.

Fig. 7. | The N-coil is exposed to antibody binding in the unloaded state of AGO1. **a**, Schematic representation of the *in vitro* binding experiment shown in **b** and **c**. **b**, Protein blots of identical amounts of immobilized, immuno-affinity purified FLAG-AGO1 variants (WT, Y691E, KKME/Y691E) incubated with the indicated concentrations of AGO1 N-coil antibody (α-AGO1-N) and competitively eluted after extensive washing. Top panel, detection with FLAG antibodies (α-FLAG) to document equal amounts of FLAG-AGO1 variants in each of the binding assays. Middle panel, detection with α-AGO1-N to document specificity of the antibody (compare AGO1^{Y691E} (intact N-coil) to AGO1$^{Y691E/}$KKME (two point mutations in N-coil) and equal reactivity towards loaded and unloaded AGO1 in the denatured state. Bottom panel, detection with anti-rabbit IgG to quantify the amount of α-AGO1-N retained by the immobilized FLAG-AGO1 variants. **c**, Quantification of the amount of α-Rabbit IgG signal in b at different α-AGO1-N concentrations. The lines show an exponential fit to the data. **d**, Immunoprecipitation of FLAG-AGO1^{WT} and FLAG-AGO^{Y691E} with α-AGO1-N antibody from total lysates of plants expressing comparable levels of FLAG-

AGO1^{WT} and FLAG-AGO^{Y691E}. The Ponceau stain of the lanes containing aliquots of total lysates shows a crop around the large subunit of RuBisCO.

Fig 8. | Structural properties, including flexibility, of the N-coil are recurrent in Ago and Piwi-clade proteins

a, Projection onto the hAgo2 model of the fractional differential hydrogen-deuterium exchange (HDX) data reported by Bibel et al. between unloaded and guide loaded hAgo2[49]. Increasing differences in exchange rate are indicated with progressively darker purple shading. All regions with differential rates of exchange between unloaded and guide-loaded hAgo2 show higher exchange rate in the unloaded state, most notably areas buried by the N-coil and engaging in interactions with N-coil residue Arg28 in the guide-loaded hAgo2. **b**, Structural overview of Siwi and Piwi outlining in pink their N-coils. The *Ephydatia fluviatilis* and *Drosophila melanogaster* Piwi proteins harbour N-coil truncations, probably generated by proteolysis during sample preparation for structural studies. **c**, Secondary structure matching of the *B. mori* and *D. melanogaster* Piwi domains reveals a more relaxed state of the *D. melanogaster* Piwi molecule (green) in which the structurally fixed N-coil seen in *B. mori* Siwi is absent.

References

1. Meister, G. Argonaute proteins: functional insights and emerging roles. *Nat Rev Genet* **14**, 447-59 (2013).
2. Czech, B. et al. piRNA-Guided Genome Defense: From Biogenesis to Silencing. *Annual Review of Genetics* **52**, 131-157 (2018).
3. Bartel, D.P. Metazoan MicroRNAs. *Cell* **173**, 20-51 (2018).
4. Ding, S.W. & Voinnet, O. Antiviral immunity directed by small RNAs. *Cell* **130**, 413-26 (2007).
5. Matzke, M.A. & Mosher, R.A. RNA-directed DNA methylation: an epigenetic pathway of increasing complexity. *Nature reviews. Genetics* **15**, 394-408 (2014).
6. Poulsen, C., Vaucheret, H. & Brodersen, P. Lessons on RNA silencing mechanisms in plants from eukaryotic argonaute structures. *Plant Cell* **25**, 22-37 (2013).
7. Qu, F., Ye, X. & Morris, J.T. Arabidopsis DRB4, AGO1, AGO7, and RDR6 participate in a DCL4-initiated antiviral RNA silencing pathway negatively regulated by DCL1 *Proc Natl Acad Sci U S A* **105**, 14732-14737 (2008).
8. Jaubert, M., Bhattacharjee, S., Mello, A.F., Perry, K.L. & Moffett, P. ARGONAUTE2 mediates RNA-silencing antiviral defenses against Potato virus X in Arabidopsis. *Plant Physiol* **156**, 1556-64 (2011).

9. Wang, X.B. et al. The 21-nucleotide, but not 22-nucleotide, viral secondary small interfering RNAs direct potent antiviral defense by two cooperative argonautes in Arabidopsis thaliana. *Plant Cell* **23**, 1625-38 (2011).
10. Carbonell, A. et al. Functional analysis of three Arabidopsis ARGONAUTES using slicer-defective mutants. *Plant Cell* **24**, 3613-29 (2012).
11. Brosseau, C. & Moffett, P. Functional and Genetic Analysis Identify a Role for Arabidopsis ARGONAUTE5 in Antiviral RNA Silencing. *The Plant Cell* **27**, 1742-1754 (2015).
12. Wang, Y., Sheng, G., Juranek, S., Tuschl, T. & Patel, D.J. Structure of the guide-strand-containing argonaute silencing complex. *Nature* (2008).
13. Schirle, N.T. & MacRae, I.J. The crystal structure of human Argonaute2. *Science* **336**, 1037-40 (2012).
14. Nakanishi, K., Weinberg, D.E., Bartel, D.P. & Patel, D.J. Structure of yeast Argonaute with guide RNA. *Nature* **486**, 368-74 (2012).
15. Elkayam, E. et al. The structure of human argonaute-2 in complex with miR-20a. *Cell* **150**, 100-10 (2012).
16. Ma, J.B. et al. Structural basis for 5'-end-specific recognition of guide RNA by the A. fulgidus Piwi protein. *Nature* **434**, 666-70 (2005).
17. Parker, J.S., Roe, S.M. & Barford, D. Structural insights into mRNA recognition from a PIWI domain–siRNA guide complex. *Nature* **434**, 663-666 (2005).
18. Ma, J.B., Ye, K. & Patel, D.J. Structural basis for overhang-specific small interfering RNA recognition by the PAZ domain. *Nature* **429**, 318-22 (2004).
19. Iki, T. et al. In vitro assembly of plant RNA-induced silencing complexes facilitated by molecular chaperone HSP90. *Mol Cell* **39**, 282-91 (2010).
20. Iwasaki, S. et al. Hsc70/Hsp90 chaperone machinery mediates ATP-dependent RISC loading of small RNA duplexes. *Mol Cell* **39**, 292-9 (2010).
21. Miyoshi, T., Takeuchi, A., Siomi, H. & Siomi, M.C. A direct role for Hsp90 in pre-RISC formation in Drosophila. *Nat Struct Mol Biol* **17**, 1024-6 (2010).
22. Iki, T., Yoshikawa, M., Meshi, T. & Ishikawa, M. Cyclophilin 40 facilitates HSP90-mediated RISC assembly in plants. *EMBO J* **31**, 267-78 (2012).
23. Iwasaki, S. et al. Defining fundamental steps in the assembly of the Drosophila RNAi enzyme complex. *Nature* (2015).
24. Matranga, C., Tomari, Y., Shin, C., Bartel, D.P. & Zamore, P.D. Passenger-strand cleavage facilitates assembly of siRNA into Ago2-containing RNAi enzyme complexes. *Cell* **123**, 607-20 (2005).
25. Rand, T.A., Petersen, S., Du, F. & Wang, X. Argonaute2 Cleaves the Anti-Guide Strand of siRNA during RISC Activation. *Cell* **123**, 621-629 (2005).
26. Leuschner, P.J.F., Ameres, S.L., Kueng, S. & Martinez, J. Cleavage of the siRNA passenger strand during RISC assembly in human cells. *EMBO reports* **7**, 314-320 (2006).
27. Endo, Y., Iwakawa, H.-o. & Tomari, Y. Arabidopsis ARGONAUTE7 selects miR390 through multiple checkpoints during RISC assembly. *EMBO reports* **14**, 652-658 (2013).
28. Reichholf, B. et al. Time-Resolved Small RNA Sequencing Unravels the Molecular Principles of MicroRNA Homeostasis. *Mol Cell* **75**, 756-768 e7 (2019).
29. Derrien, B. et al. Degradation of the antiviral component ARGONAUTE1 by the autophagy pathway. *Proc Natl Acad Sci U S A* **109**, 15942-6 (2012).

30. Smibert, P., Yang, J.-S., Azzam, G., Liu, J.-L. & Lai, E.C. Homeostatic control of Argonaute stability by microRNA availability. *Nature Structural & Molecular Biology* **20**, 789-795 (2013).
31. Martinez, N.J. & Gregory, R.I. Argonaute2 expression is post-transcriptionally coupled to microRNA abundance. *RNA* **19**, 605-612 (2013).
32. Johnston, M., Geoffroy, M.-C., Sobala, A., Hay, R. & Hutvagner, G. HSP90 Protein Stabilizes Unloaded Argonaute Complexes and Microscopic P-bodies in Human Cells. *Molecular Biology of the Cell* **21**, 1462-1469 (2010).
33. Gibbings, D. et al. Selective autophagy degrades DICER and AGO2 and regulates miRNA activity. *Nat Cell Biol* **14**, 1314-21 (2012).
34. Kobayashi, H., Shoji, K., Kiyokawa, K., Negishi, L. & Tomari, Y. VCP Machinery Mediates Autophagic Degradation of Empty Argonaute. *Cell Reports* **28**, 1144-1153.e4 (2019).
35. Kobayashi, H., Shoji, K., Kiyokawa, K., Negishi, L. & Tomari, Y. Iruka Eliminates Dysfunctional Argonaute by Selective Ubiquitination of Its Empty State. *Molecular Cell* **73**, 119-129.e5 (2019).
36. Hacquard, T. et al. The Arabidopsis F-box protein FBW2 targets AGO1 for degradation to prevent spurious loading of illegitimate small RNA. *Cell Reports* **39**(2022).
37. Gregory, B.D. et al. A link between RNA metabolism and silencing affecting Arabidopsis development. *Dev Cell* **14**, 854-66 (2008).
38. Brodersen, P. et al. Isoprenoid biosynthesis is required for miRNA function and affects membrane association of ARGONAUTE 1 in Arabidopsis. *Proc Natl Acad Sci U S A* **109**, 1778-83 (2012).
39. Fang, X., Cui, Y., Li, Y. & Qi, Y. Transcription and processing of primary microRNAs are coupled by Elongator complex in Arabidopsis. *Nature Plants* **1**, 15075 (2015).
40. Hauptmann, J. et al. Turning catalytically inactive human Argonaute proteins into active slicer enzymes. *Nature Structural & Molecular Biology* **20**, 814-817 (2013).
41. Honig, A., Avin-Wittenberg, T., Ufaz, S. & Galili, G. A new type of compartment, defined by plant-specific Atg8-interacting proteins, is induced upon exposure of Arabidopsis plants to carbon starvation. *Plant Cell* **24**, 288-303 (2012).
42. Sjøgaard, I.M.Z. et al. The transmembrane autophagy cargo receptors ATI1 and ATI2 interact with ATG8 through intrinsically disordered regions with distinct biophysical properties. *Biochemical Journal* **476**, 449-465 (2019).
43. Michaeli, S. et al. The viral F-box protein P0 induces an ER-derived autophagy degradation pathway for the clearance of membrane-bound AGO1. *Proceedings of the National Academy of Sciences* **116**, 22872-22883 (2019).
44. Petersen, N.H.T. et al. Identification of proteins interacting with Arabidopsis ACD11. *Journal of Plant Physiology* **166**, 661-666 (2009).
45. Craxton, M. Evolutionary genomics of plant genes encoding N-terminal-TM-C2 domain proteins and the similar FAM62 genes and synaptotagmin genes of metazoans. *BMC Genomics* **8**, 259 (2007).
46. Rudel, S. et al. Phosphorylation of human Argonaute proteins affects small RNA binding. *Nucleic Acids Res* **39**, 2330-43 (2011).
47. Li, S. et al. MicroRNAs inhibit the translation of target mRNAs on the endoplasmic reticulum in Arabidopsis. *Cell* **153**, 562-74 (2013).

48. Sjögren, L. et al. Farnesylated heat shock protein 40 is a component of membrane-bound RISC in Arabidopsis. *Journal of Biological Chemistry* **293**, 16608-16622 (2018).
49. Bibel, B., Elkayam, E., Silletti, S., Komives, E.A. & Joshua-Tor, L. Target binding triggers hierarchical phosphorylation of human Argonaute-2 to promote target release. *eLife* **11**, e76908 (2022).
50. Brennecke, J. et al. Discrete small RNA-generating loci as master regulators of transposon activity in Drosophila. *Cell* **128**, 1089-103 (2007).
51. Gunawardane, L.S. et al. A slicer-mediated mechanism for repeat-associated siRNA 5' end formation in Drosophila. *Science* **315**, 1587-90 (2007).
52. Brennecke, J. et al. An Epigenetic Role for Maternally Inherited piRNAs in Transposon Silencing. *Science* **322**, 1387-1392 (2008).
53. Sato, K. et al. Krimper Enforces an Antisense Bias on piRNA Pools by Binding AGO3 in the Drosophila Germline. *Molecular Cell* **59**, 553-563 (2015).
54. Weiberg, A. et al. Fungal small RNAs suppress plant immunity by hijacking host RNA interference pathways. *Science* **342**, 118-23 (2013).
55. Hou, Y. et al. A Phytophthora Effector Suppresses Trans-Kingdom RNAi to Promote Disease Susceptibility. *Cell Host & Microbe* **25**, 153-165.e5 (2019).
56. Shahid, S. et al. MicroRNAs from the parasitic plant Cuscuta campestris target host messenger RNAs. *Nature* **553**, 82-85 (2018).
57. Buck, A.H. et al. Exosomes secreted by nematode parasites transfer small RNAs to mammalian cells and modulate innate immunity. *Nature Communications* **5**, 5488 (2014).
58. Krissinel, E. & Henrick, K. Inference of Macromolecular Assemblies from Crystalline State. *Journal of Molecular Biology* **372**, 774-797 (2007).

On-line content

Methods, Supplemental Figures 1-13, Supplemental Tables 1-2, additional references supporting Methods and legends of supplemental figures and tables.

Data availability

NMR data have been deposited at the Biological Magnetic Resonance Bank (BMRB) under BMRB entry 51660.

Code availability

The study did not develop new code. Standard procedures for mathematical and statistical analysis of data are described in Methods.

Acknowledgements

Theo Bølsterli and his team are thanked for plant care and Signe A. Sjørup for assistance with MALDI-TOF experiments and purification of proteins. We thank Laura Arribas-Hernández and Diego López-Marquez for critical reading of the manuscript.

Funding

This work was supported by a Hallas Møller Stipend (Hallas Møller 2010) and a project grant (NNF17OC0029194) from the Novo Nordisk Foundation, and Starting (ERC-2011-StG 282460 MICROMECCA) and Consolidator Grants (ERC-2016-CoG 726417 PATHORISC) from the European Research Council, all to PB. The work was also supported by the Novo Nordisk Foundation Challenge program (REPIN; grant number NNF18OC0033926 to BBK). The NMR spectra were recorded at cOpenNMR, an infrastructure initiative supported by the Novo Nordisk Foundation grant number NNF18OC0032996.

Author contributions

SB constructed plant lines expressing unloaded FLAG-AGO1 and its combinations with N-coil mutants in *ago1-3* knockout backgrounds, conducted bimolecular fluorescence complementation analyses, pulse-labeling experiments and resulting data analysis, developed the AGO1 N-coil antibody and conducted binding experiments and subsequent data analysis. IMZB expressed and purified recombinant proteins, conducted MST assays with SB and NMR experiments with AP, developed the ATI1 antibody, and participated with SB in preliminary tests and AGO1 binding experiments with a lower-affinity N-coil antibody not used in the final experiments reported here. SK conducted two-hybrid screening and initial mutational analysis of AGO1 NcGN, further developed by AM. EDO set up CRISPR-Cas9 engineering, isolated *ati2* mutant alleles in Col-0, constructed *ati1/ati2* double mutants, and some transgenic lines expressing N-coil mutants of AGO1 in *ago1-3* knockout backgrounds. CP conducted analysis of structures and suggested that the N-coil may adopt conformations different from the one seen in crystal structures of HsAgo2. BBK helped design NMR experiments, and, together with AP, supervised all work and data analysis related to those experiments. PB designed and supervised the study and wrote the manuscript with contributions from all authors.

Competing interests

The authors declare no competing interests.

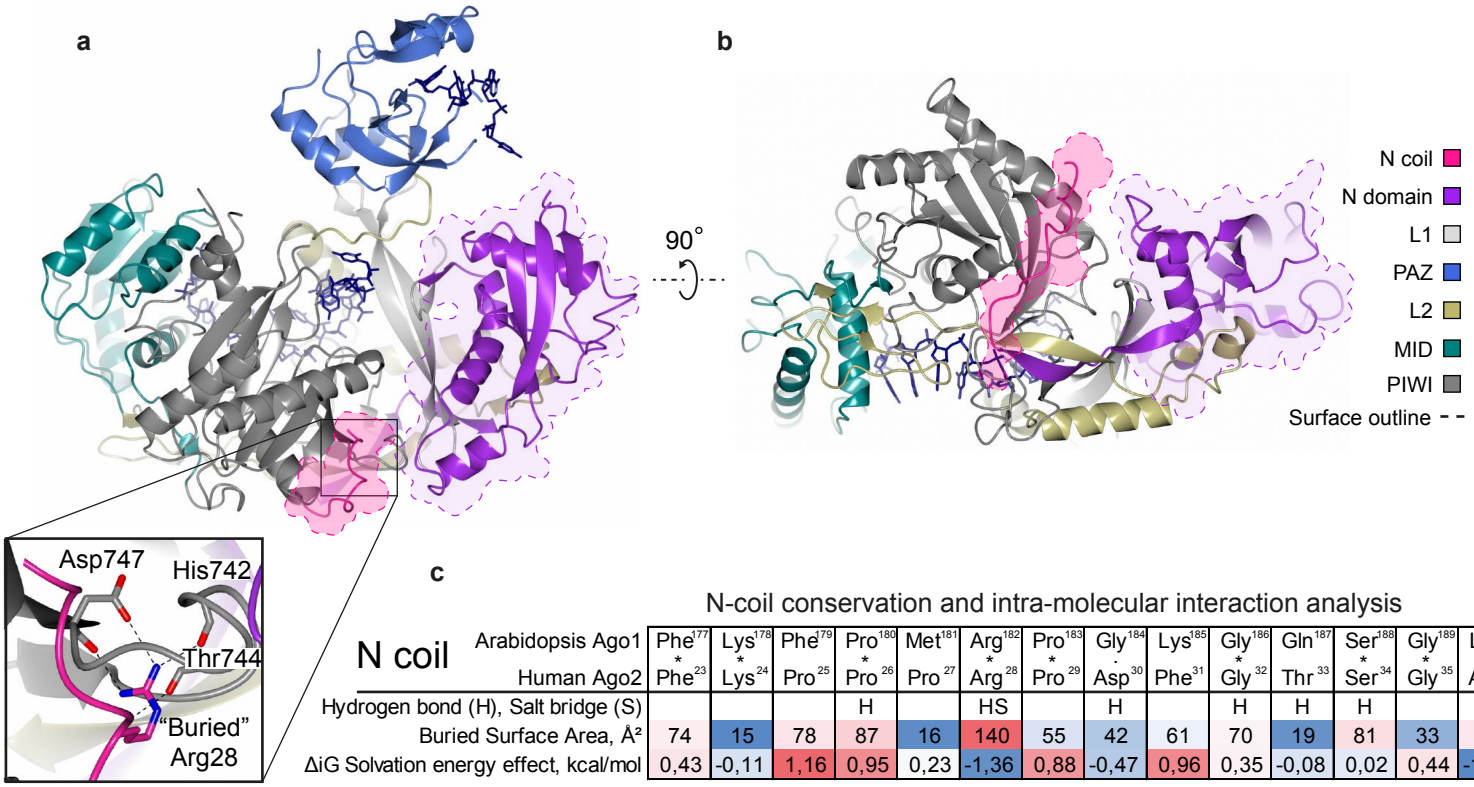

c

N-coil conservation and intra-molecular interaction analysis

N coil	Arabidopsis Ago1	Phe^{177}	Lys^{178}	Phe^{179}	Pro^{180}	Met^{181}	Arg^{182}	Pro^{183}	Gly^{184}	Lys^{185}	Gly^{186}	Gln^{187}	Ser^{188}	Gly^{189}	Lys^{190}
	Human Ago2	Phe^{23}	Lys^{24}	Pro^{25}	Pro^{26}	Pro^{27}	Arg^{28}	Pro^{29}	Asp^{30}	Phe^{31}	Gly^{32}	Thr^{33}	Ser^{34}	Gly^{35}	Arg^{36}
Hydrogen bond (H), Salt bridge (S)					H		HS		H		H	H	H		HS
Buried Surface Area, Å²		74	15	78	87	16	140	55	42	61	70	19	81	33	76
ΔiG Solvation energy effect, kcal/mol		0,43	-0,11	1,16	0,95	0,23	-1,36	0,88	-0,47	0,96	0,35	-0,08	0,02	0,44	-1,48

Fig. 1 | Structural properties and conserved interactions of the N-coil in Hs-Ago2. Overview of the Hs-Ago2 domain structure with surface outline of the globular N domain and the N-coil. **a**, "side view"; **b**, "bottom view". **c**, Intra-molecular interactions between the N-coil and the remaining part of Hs-Ago2 as calculated by the Protein Interfaces, Surfaces and Assemblies service PISA[58]. The solvation energy gain of the N-coil is calculated as the difference between free energy of the associated and the dissociated N-coil. A negative solvation energy, $\Delta_i G$, of a residue makes a positive contribution to the solvation energy gain of the interface thus favoring the dissociated state. The color gradient (blue to red) indicates the effect sizes of buried surface area and solvation energy and highlights the unique properties of Arg-28. **d**, Inlet showing conserved residues and bonds between a buried arginine side chain in the N-coil (R28 in Hs-Ago2) and nearby residues. Data and presentations were made using the crystal structure coordinates of the miR20a-bound Hs-Ago2 (PDB 4F3T)[15].

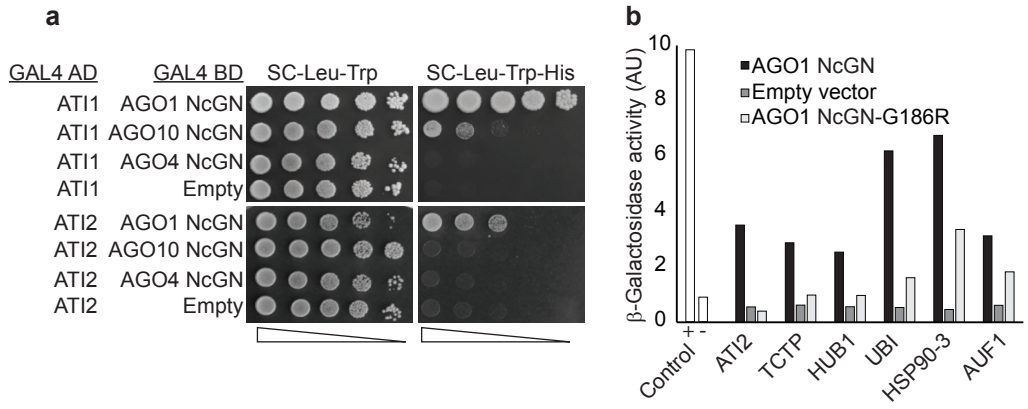

Fig. 2 | Interactions with AGO1-NcGN are specific and often require an intact N-coil. a, Yeast two-hybrid analysis of ATI1 and ATI2 fused to the activation domain (AD) of the yeast transcription factor Gal4 co-expressed either with NcGN domains of AGO1/AGO10/AGO4 fused to the DNA binding domain of Gal4 (BD), or with Gal4-BD alone (empty). 10-fold serial dilutions of yeast cells were spotted on permissive (left) and selective (right) media. **b**, β-galactosidase activity measured in an *ortho*-nitrophenyl-β-galactoside (ONPG) assay conducted with total protein lysates prepared from yeast strains expressing each candidate fused to Gal4-AD and AGO1-NcGN-Gal4-BD, AGO1-NcGN^{G186R}-Gal4-BD, or unfused Gal4-BD (empty). y-axis shows β-galactosidase activity in arbitrary units. The yeast Swi2-Swi6 interaction was used as positive control, and co-expression of unfused Gal4-AD and Gal4-BD was used as negative control.

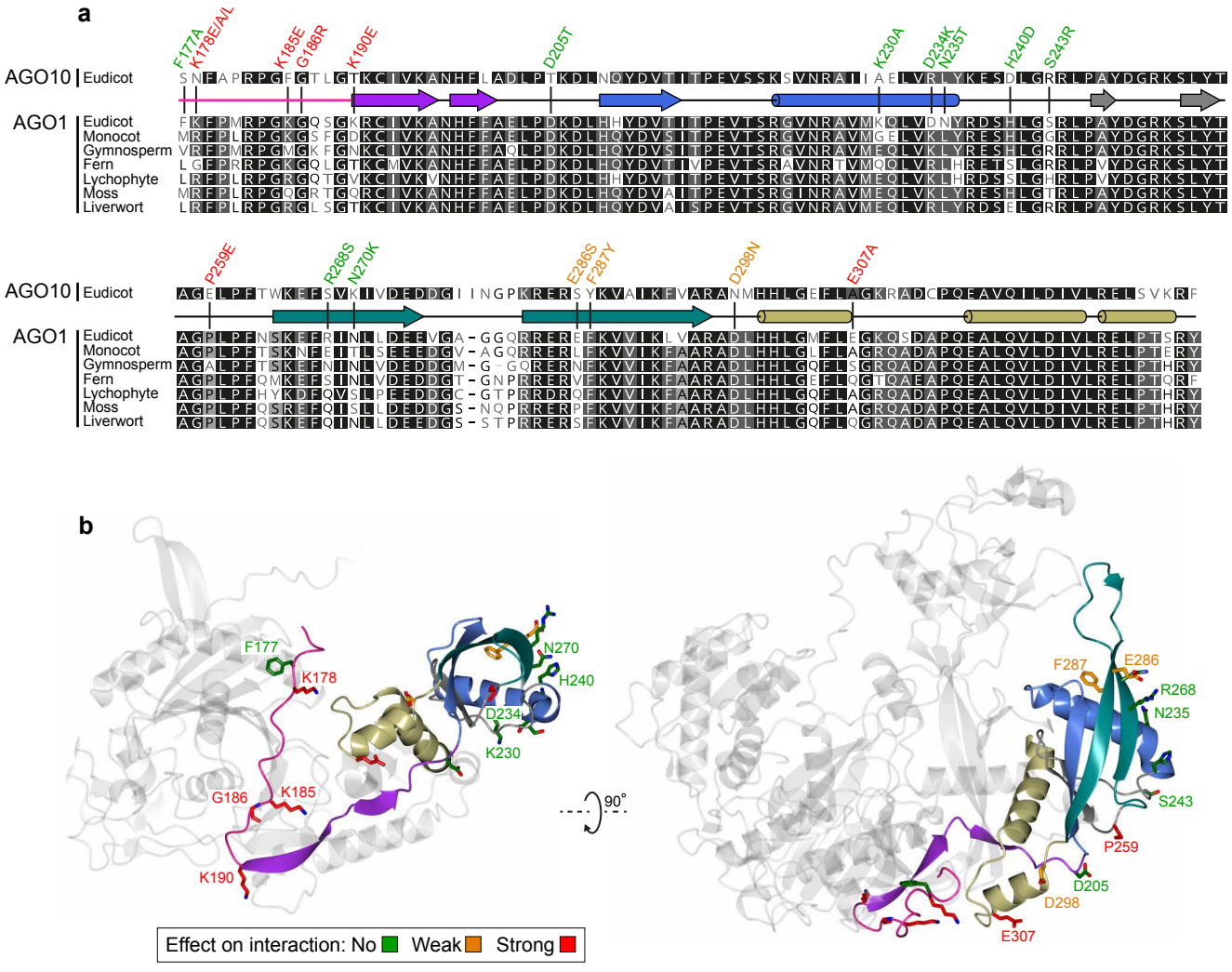

Fig. 3 | Residues required for ATI1/ATI2 interaction cluster in the N-coil and in surface-exposed patches of the globular N-domain. a, Sequence alignments of the *Arabidopsis* paralogs AGO1 and AGO10, and of orthologs of *Arabidopsis* AGO1 from plant species representing major phylogenetic groups of land plants. The species chosen from the different groups were as follows: Liverwort, *Marchantia polymorpha*; moss, *Ceratodon purpureus*; lycophyte, *Selaginella moellendorfii*; fern; *Ceratopteris richardii*; gymnosperm, *Pinus tabuliformis*; monocot, *Elaeis guineensis*; dicot, *Arabidopsis thaliana*. Residues selected for mutational analysis are marked on the alignment. **b**, Alphafold ribbon model of *Arabidopsis* AGO1 with the N-coil and N domain highlighted in rainbow colors. The residues studied by mutation are presented in sticks and colored according to the effect of mutation on ATI1/ATI2 interaction with AGO1-NcGN in the yeast two-hybrid assay. The underlying evidence from yeast-two hybrid spotting assays is shown in Supplemental Fig. 7-8.

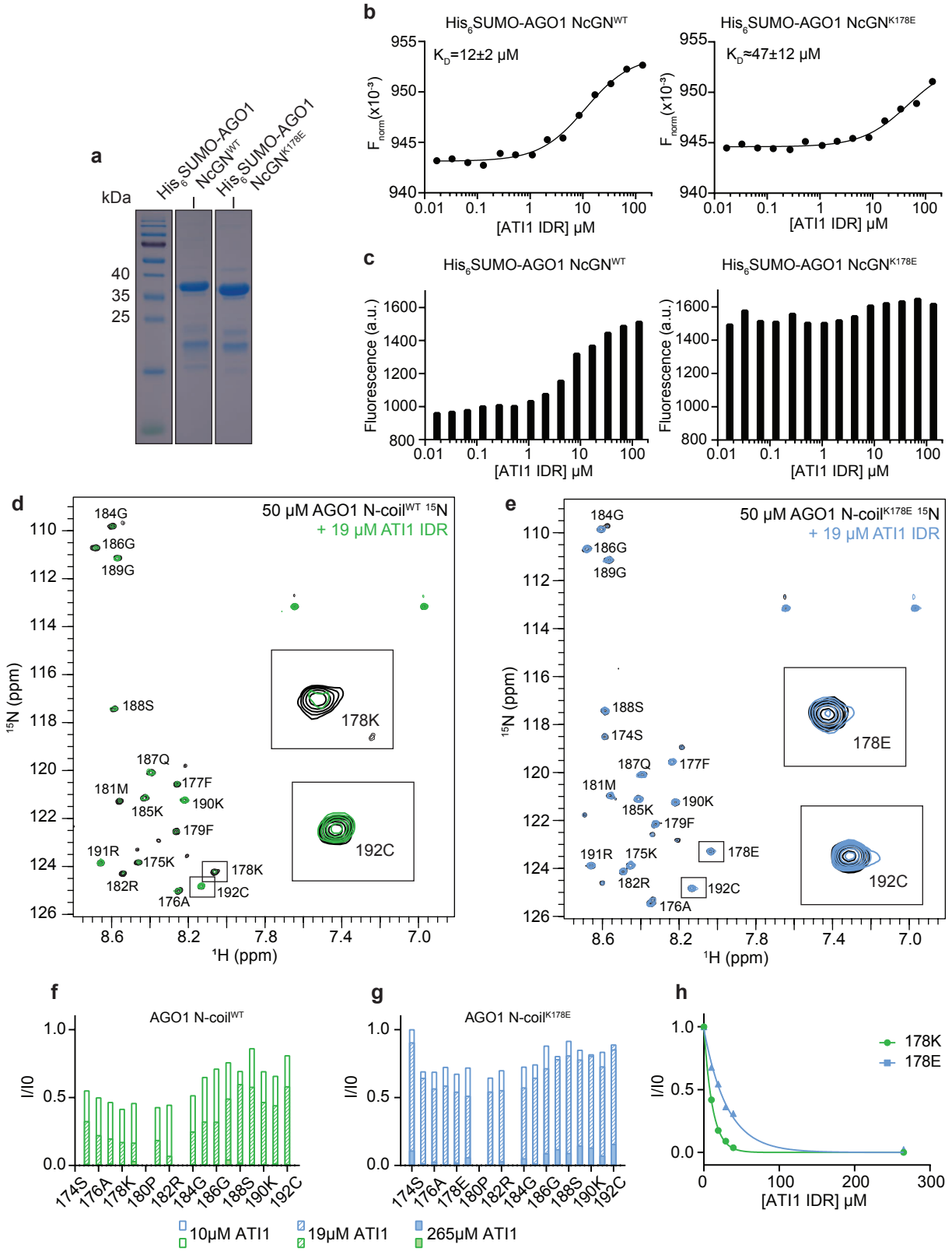

Fig. 4 | The N-coil is a direct binding site for ATI1 *in vitro*. **a**, SDS-PAGE of heterologously expressed His_6SUMO-AGO1-NcGN protein used for fluorescence labeling and microscale thermophoresis (MST) assays. **b**, MST measurements of fluorescence intensity of His_6SUMO-AGO1 NcGN WT (left) and K178E (right) after application of a temperature gradient. Fluorescence data obtained from the thermophoretic acquisition period were normalized to the initial fluorescence before being fitted to a one-site binding curve with increasing concentrations of ATI1-IDR. The reported binding constants (K_D) are calculated with standard errors. **c**, Simple fluorescence intensity of Cys192-labeled His_6SUMO-AGO1 NcGN WT (left) and K178E (right) as a function of the concentration of ATI1-IDR. **d, e**, ^{1}H,^{15}N-HSQC nuclear magnetic resonance spectra of 50 μM of ^{15}N-labeled AGO1 N-coil WT (left, black) or K178E peptide (right, black), with 19 μM ATI1-IDR added (green with N-coil WT, blue with N-coil K178E). Zooms of contour levels of residues K178 and C192 are highlighted in the boxes. Minor peaks were assigned to a C-terminally truncated version of the AGO1 N-coil peptide whose presence in the sample was verified by MALDI-TOF mass spectrometry. **f, g**, Peak intensity plots of ^{15}N-labeled AGO1 N-coil peptide (50 μM) upon titration of ATI1-IDR. Peak intensities are normalized to peak intensities observed with free AGO1 N-coil peptide. **h**, Peak intensity of residues K178 (for the AGO1 wild type N-coil, green) and E178 (for the K178E N-coil mutant, blue) as a function of the ATI1-IDR concentration. The data points are fitted to an exponential function.

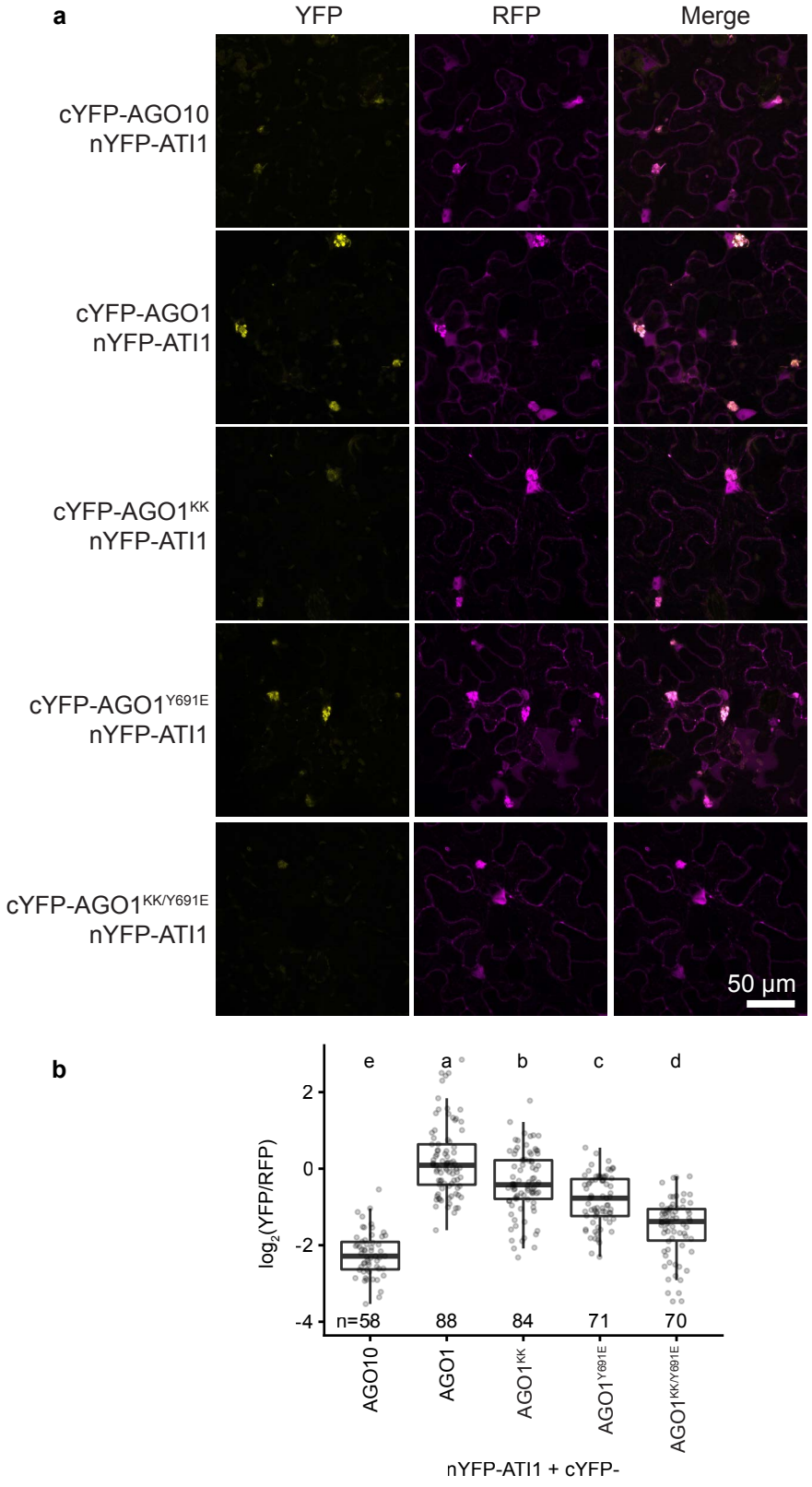

Fig. 5 | Unloaded AGO1 interacts with ATI1 *in vivo*. a, Confocal images showing results of bimolecular fluorescence complementation (BiFC) assays to probe the AGO1-ATI1 interaction *in vivo*. The C-terminal half of YFP was fused to AGO10, or to wild type or unloaded (Y691E) AGO1 with either an intact or a mutated (K185E/K190E) N-coil. The N-terminal half of YFP was fused to ATI1. Both fused halves of YFP were expressed from the same plasmid also expressing free RFP. For each BiFC pair, possible interaction is detected by fluorescence from reconstituted YFP. RFP fluorescence serves as a control for transformation. Merged channel images demonstrate the presence of yellow fluorescence only in transformed cells. Scale bar, 50 µm. **b**, Quantification of YFP signal normalized to RFP signal in the given number of YFP-positive cells for the interactions shown in a. Letters indicate groups with statistically significantly different $\log_2$(YFP/RFP) ratios ($p < 0.05$; ANOVA with post-hoc Tukey Honestly Significant Difference test). See Supplemental Fig. 9 for evidence that AGO1^{Y691E} is unloaded, and Supplemental Fig. 10 for image data underlying the quantification in b. KK, K185E/K190E.

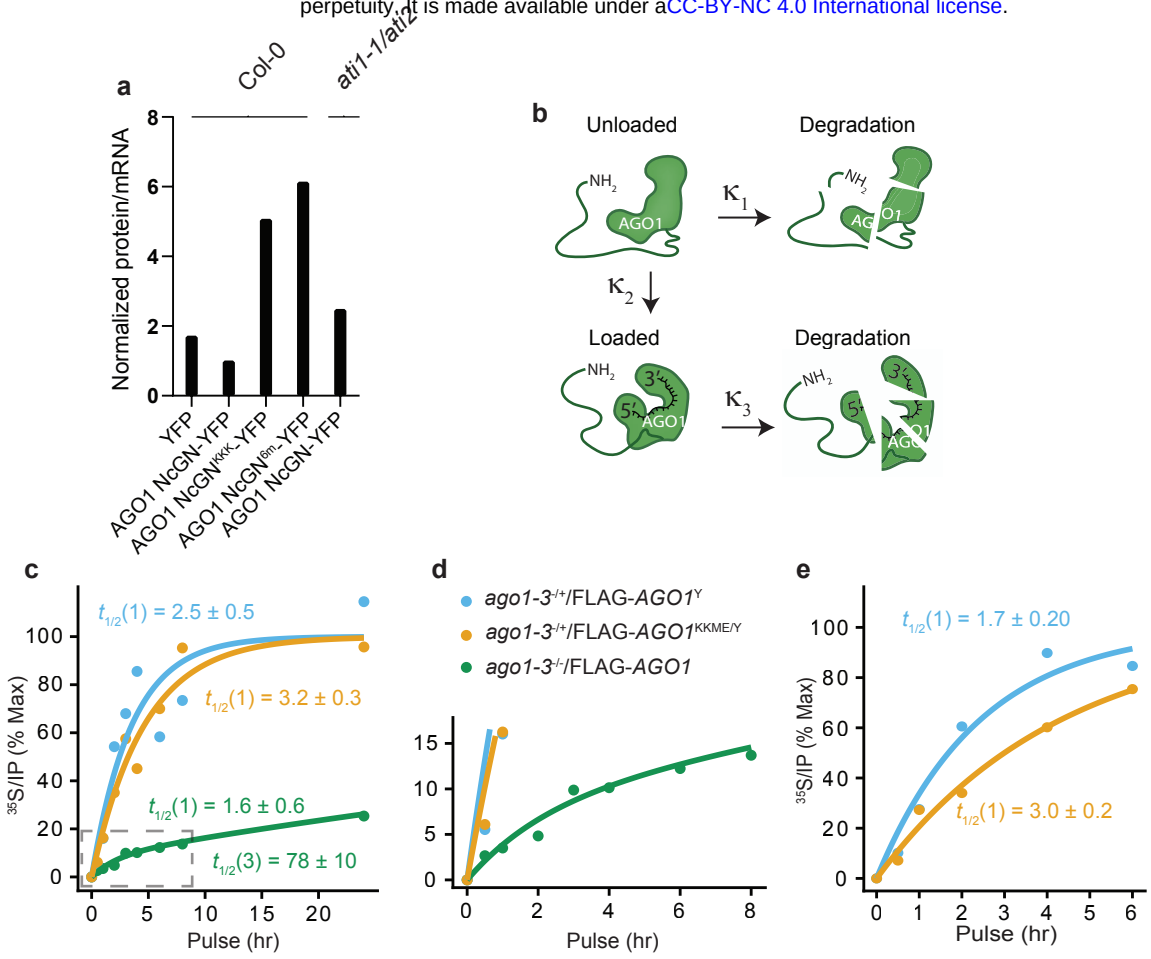

Fig. 6 | An intact AGO1 N-coil is required for maximal turnover rate of unloaded AGO1 *in vivo*. **a**, Ratios of normalized YFP protein to YFP mRNA levels as quantified by protein and RNA blots in stable transgenic lines constitutively expressing AGO1 NcGN-YFP fusions, either in WT or in the *ati1-1/ati2* knock-out background. Ratios are normalized to AGO1-NcGN^{WT}-YFP expressed in WT. KKK, K178E/K185E/K190E; 6mut, KKK/P259E/M304E/E307A. **b**, Kinetic model of the two different fates of newly synthesized AGO1: direct degradation (κ_1), or small RNA loading (κ_2) followed by degradation (κ_3). **c**, Quantification of ^{35}S-Met/Cys incorporation into FLAG-AGO1^{WT}, FLAG-AGO1^{Y691E} or FLAG-AGO1$^{KKME/Y691E}$ as a function of pulse time. The lines represent a fit to an exponential equation for unloadable AGO1 containing the Y691E mutation and a fit to a double exponential equation for the WT AGO1. The half-lives calculated by the fitted models are given in hours +/- standard deviation, as detailed in Methods. **d**, Zoom in of the dashed area of **c**. **e**, Result of an independent experiment done as in **c** to verify the slower incorporation kinetics in FLAG-AGO1$^{KKME/Y691E}$ compared to FLAG-AGO1^{Y691E}. See Supplemental Fig. 11 for protein and RNA blot data underlying Fig. 6a, and Supplemental Fig. 12 for raw data underlying Fig. 6c-e.

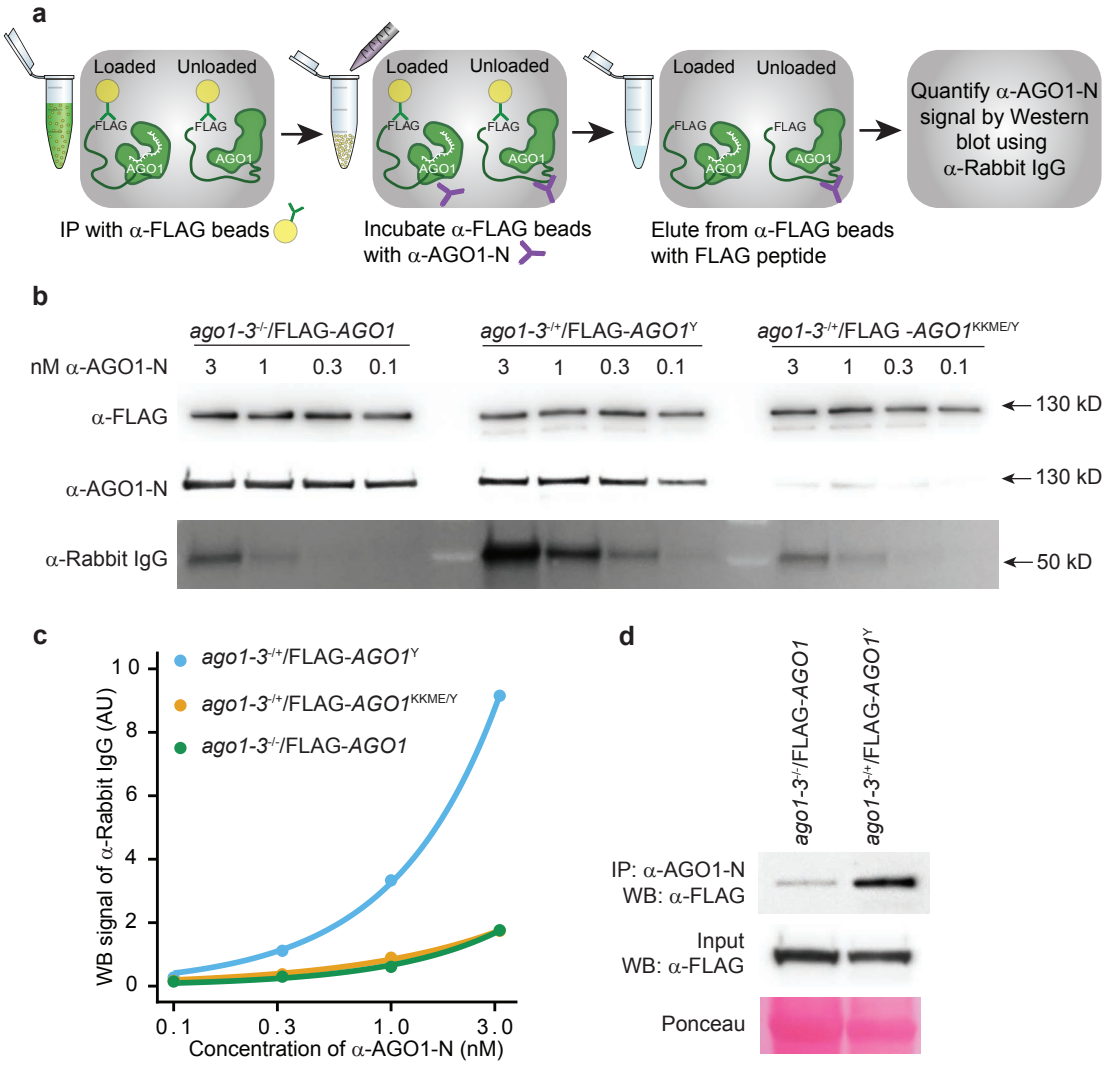

Fig. 7. | The N-coil is exposed to antibody binding in the unloaded state of AGO1. **a**, Schematic representation of the *in vitro* binding experiment shown in **b** and **c**. **b**, Protein blots of identical amounts of immobilized, immuno-affinity purified FLAG-AGO1 variants (WT, Y691E, KKME/Y691E) incubated with the indicated concentrations of AGO1 N-coil antibody (α-AGO1-N) and competitively eluted after extensive washing. Top panel, detection with FLAG antibodies (α-FLAG) to document equal amounts of FLAG-AGO1 variants in each of the binding assays. Middle panel, detection with α-AGO1-N to document specificity of the antibody (compare AGO1^{Y691E} (intact N-coil) to AGO1$^{Y691E/}$KKME (two point mutations in N-coil) and equal reactivity towards loaded and unloaded AGO1 in the denatured state. Bottom panel, detection with anti-rabbit IgG to quantify the amount of α-AGO1-N retained by the immobilized FLAG-AGO1 variants. **c**, Quantification of the amount of α-Rabbit IgG signal in b at different α-AGO1-N concentrations. The lines show an exponential fit to the data. **d**, Immunoprecipitation of FLAG-AGO1^{WT} and FLAG-AGO^{Y691E} with α-AGO1-N antibody from total lysates of plants expressing comparable levels of FLAG-AGO1^{WT} and FLAG-AGO^{Y691E}. The Ponceau stain of the lanes containing aliquots of total lysates shows a crop around the large subunit of RuBisCO.

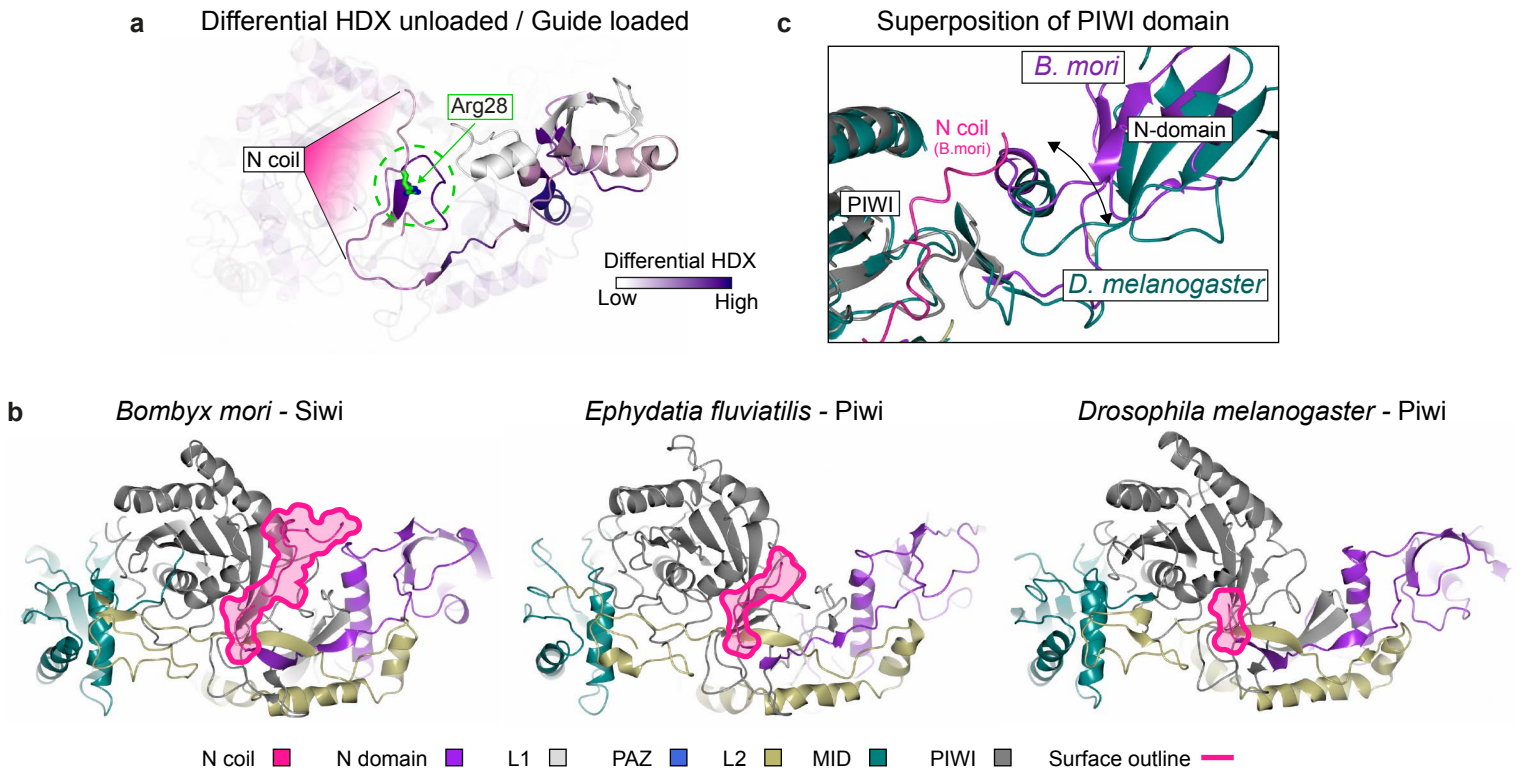

Fig 8. | Structural properties, including flexibility, of the N-coil are recurrent in Ago and Piwi-clade proteins. a, Projection onto the hAgo2 model of the fractional differential hydrogen-deuterium exchange (HDX) data reported by Bibel et al. between unloaded and guide loaded hAgo2[49]. Increasing differences in exchange rate are indicated with progressively darker purple shading. All regions with differential rates of exchange between unloaded and guide-loaded hAgo2 show higher exchange rate in the unloaded state, most notably areas buried by the N-coil and engaging in interactions with N-coil residue Arg28 in the guide-loaded hAgo2. **b**, Structural overview of Siwi and Piwi outlining in pink their N-coils. The *Ephydatia fluviatilis* and *Drosophila melanogaster* Piwi proteins harbour N-coil truncations, probably generated by proteolysis during sample preparation for structural studies. **c**, Secondary structure matching of the *B. mori* and *D. melanogaster* Piwi domains reveals a more relaxed state of the *D. melanogaster* Piwi molecule (green) in which the structurally fixed N-coil seen in *B. mori* Siwi is absent.